American Society of Mechanical Engineers

ASME Accepted Manuscript Repository

Institutional Repository Cover Sheet

Michele Sergio   Campobasso

First   *Last*

ASME Paper Title: Analysis of Unsteady Flows Past Horizontal Axis Wind Turbine Airfoils Based on Harmonic Balance

Compressible Navier-Stokes Equations With Low-Speed Preconditioning

Authors: M. Sergio Campobasso and Mohammad H. Baba-Ahmadi

*VOR (version of record)

ANALYSIS OF UNSTEADY FLOWS PAST HORIZONTAL AXIS WIND TURBINE AIRFOILS BASED ON HARMONIC BALANCE COMPRESSIBLE NAVIER-STOKES EQUATIONS WITH LOW-SPEED PRECONDITIONING

M. Sergio Campobasso[*]

School of Engineering

James Watt Building South, University Avenue

University of Glasgow

Glasgow G12 8QQ, United Kingdom

Email: sergio.campobasso@glasgow.ac.uk

Mohammad H. Baba-Ahmadi

School of Engineering

James Watt Building South, University Avenue

University of Glasgow

Glasgow G12 8QQ, United Kingdom

Email: m.baba-ahmadi@aero.gla.ac.uk

ABSTRACT

This paper presents the numerical models underlying the implementation of a novel harmonic balance compressible Navier-Stokes solver with low-speed preconditioning for wind turbine unsteady aerodynamics. The numerical integration of the harmonic balance equations is based on a multigrid iteration, and, for the first time, a numerical instability associated with the use of such an explicit approach in this context is discussed and resolved. The harmonic balance solver with low-speed preconditioning is well suited for the analyses of several unsteady periodic low-speed flows, such as those encountered in horizontal axis wind turbines. The computational performance and the accuracy of the technology being developed are assessed by computing the flow field past two sections of a wind turbine blade in yawed wind with both the time- and frequency-domain solvers. Results highlight that the harmonic balance solver can compute these periodic flows more than 10 times faster than its time-domain counterpart, and with an accuracy comparable to that of the time-domain solver.

INTRODUCTION

The aeromechanical design of horizontal axis wind turbines (HAWT's) is a complex multidisciplinary task that requires consideration of a very large number of operating regimes due to the extreme variability of the environmental conditions on time scales

---

[*]Address all correspondence to this author.

ranging from seconds (*e.g.* wind gusts) to months (*e.g.* seasonal wind variations). Modern industrial design still relies on low-fidelity and/or semi-empirical computational tools such as blade element momentum theory (BEMT), stall and dynamic inflow models [1]. The main advantage of these techniques is their high computational speed. Their main drawback is that they heavily rely on the existence and availability of high-quality airfoil data. Thus, new HAWT configurations cannot be assessed with confidence by means of these methods. Conversely, the use of high-fidelity computational aerodynamics tools such as Navier-Stokes (NS) solvers in an integrated aeromechanical analysis and design system has the potential of overcoming the aforementioned constraint. These solvers enable one to analyze the unsteady aerodynamic and aeroelastic response of prospective new turbine configurations to challanging off-design conditions. Several outstanding examples of the predictive capabilities of NS solvers for HAWT aerodynamics have been published [2–4]. The main drawback of NS solvers is their computational cost, which is substantially higher than that of low-fidelity systems even when massive parallel computing is adopted. Accurate time-dependent simulations of HAWT flows may still take several days, whereas the same engineering problem could be solved within a few hours using BEMT-based systems.

Several fundamental HAWT unsteady aerodynamic problems can be viewed as periodic. This is the case of stall-induced vibrations and the yawed wind regime, which occurs when the freestream wind velocity is not orthogonal to the turbine rotor. The yawed wind problem is one for which the underlying assumptions of BEMT-based systems are particularly weak, and a more reliable analysis of which would therefore benefit from the use of unsteady NS solvers. A time-resolved time-domain (TD) NS simulation of this problem requires a long wallclock time due to the fact that several rotor revolutions have to be simulated before a periodic state is achieved, and a time-resolved solution requires about 1000 physical time steps per revolution [5]. Fortunately, the wallclock time required by the TD NS prediction of unsteady periodic flows can be dramatically reduced by using a frequency-domain (FD) formulation and solution of the governing unsteady equations. The harmonic balance (HB) NS technology for the solution of unsteady periodic flows [6] is one of the most promising FD NS methods. The HB NS technology has been applied to the prediction of the periodic flow associated with flutter and forced response of turbomachinery blades [6–8], and various vibratory motion modes of aircraft configurations [9–11]. For this type of application, it has been observed that the use of the HB NS approach for the calculation of periodic flows can lead to a reduction of the wallclock time varying between one and two orders of magnitude with respect to conventional TD NS analyses. Another successful and computationally effective FD approach to the solution of unsteady periodic flows is the nonlinear frequency-domain (NLFD) method [12–14]. The NLFD technology has also been applied to the simulation of the periodic flow past rotorcraft blades [15]. Several other FD methods have been developed in the past years, among which a one-harmonic FD technique for the calculation of periodic turbomachinery flows [16], which bears some resemblance to the HB approach of [6], but differs from it in that the calculation of the zeroth harmonic (mean state) is decoupled from that of the first harmonic representing the sought unsteady flow component. Numerous examples of the application of the HB and NLFD technologies to periodic flows of engineering interest exist, but a thorough review of all existing FD methods and their application is beyond the scope of this report.

This paper focuses on the development and application of the HB NS technology for the analysis of periodic wind turbine flows, such as that caused by the yawed wind condition. One of the main differences between HAWT flows and the other aerodynamic

problems for which the HB NS method has been used thus far is that the flow speeds observed in wind turbine flows are typically in the incompressible range (Mach number well below 0.3), though future large off-shore turbines are likely to operate at the border between the incompressible and compressible regimes. A NS solver for HAWT aerodynamics could therefore be based either on the incompressible formulation or the compressible formulation augmented with *low-speed preconditioning* (LSP) [17, 18]. One of the advantages of choosing the compressible formulation with LSP is the capability of this approach to perform aeroacoustic analyses.

This paper presents the mathematical and numerical theory behind the implementation of a time- and frequency-domain multigrid (MG) compressible NS solver based on the HB technology and featuring an optimized LSP method. It also discusses an important numerical stability problem that may be encountered when solving the HB NS equations with explicit solvers such as the MG iteration based on the Runge-Kutta smoother, and it proposes a robust and elegant solution for suppressing such an instability. Then, a simple kinematic model enabling one to determine the two-dimensional (2D) time-dependent freestream conditions observed by the blade sections of a HAWT in yawed wind is presented. Finally, the effectiveness of the HB NS solver with LSP is demonstrated by computing the periodic unsteady flow past two sections of a HAWT blade in yawed wind using both the TD and the HB solvers. The TD and HB results are compared in terms of accuracy and wallclock time required for their calculation. To the best of the authors' knowledge, this is the first reported development of the NS HB technology with LSP and its application to wind turbine unsteady aerodynamics.

GOVERNING EQUATIONS

Time-domain formulation

Internal and external viscous flows can be computed by solving the NS equations, which are a system of N_{pde} nonlinear partial differential equations (PDE's) obtained by imposing the conservation of mass, momentum and energy over a control volume. For 2D laminar flows $N_{pde} = 4$ because the momentum equation has only two scalar components. Given a control volume $\mathcal{C}$ with boundary S, the Arbitrary Lagrangian-Eulerian (ALE) integral form of the 2D TD NS equation is:

$$\frac{\partial}{\partial t} \left(\int_{C(t)} \mathbf{U} \, dC \right) + \oint_{S(t)} (\underline{\Phi}_i - \underline{\Phi}_v) \cdot d\underline{S} = 0 \tag{1}$$

The array $\mathbf{U}$ of conservative flow variables is defined as:

$$\mathbf{U} = [\rho \;\; \rho u \;\; \rho v \;\; \rho \varepsilon]'$$

where the superscript $'$ denotes the transpose operator, and ρ, u, v and ε are respectively the flow density, the $x-$ and $y-$component of the flow velocity vector $\underline{v}$, and the total energy per unit mass. The definition of the total energy is $\varepsilon = e + (u^2 + v^2)/2$, where e denotes the internal energy per unit mass. The generalized inviscid flux vector $\underline{\Phi}_i$ is:

$$\underline{\Phi}_i = \mathbf{E}_i \underline{i} + \mathbf{F}_i \underline{j} - \underline{v}_b \mathbf{U} \tag{2}$$

where $\mathbf{E}_i$ and $\mathbf{F}_i$ are respectively the $x-$ and $y-$components of $\underline{\Phi}_i$, and are given by:

$$\mathbf{E}_i = [\rho u \quad \rho u^2 + p \quad \rho u v \quad \rho u H]' \,, \qquad \mathbf{F}_i = [\rho v \quad \rho u v \quad \rho v^2 + p \quad \rho v H]'$$

The vector $\underline{v}_b$ is the velocity of the boundary S, and the flux term $-\underline{v}_b \mathbf{U}$ is its contribution to the overall flux balance, which is nonzero only in the case of unsteady problems with moving boundaries. The symbol p denotes the static pressure and the symbol H denotes the total enthalpy per unit mass, the expression of which is $H = \varepsilon + p/\rho$. The generalized viscous flux vector $\underline{\Phi}_v$ is:

$$\underline{\Phi}_v = \mathbf{E}_v \underline{i} + \mathbf{F}_v \underline{j} \tag{3}$$

where $\mathbf{E}_v$ and $\mathbf{F}_v$ are respectively the $x-$ and $y-$components of $\underline{\Phi}_v$, and are given by:

$$\mathbf{E}_v = \begin{bmatrix} 0 \\ \tau_{xx} \\ \tau_{xy} \\ u\tau_{xx} + v\tau_{xy} - q_x \end{bmatrix} \,, \qquad \mathbf{F}_v = \begin{bmatrix} 0 \\ \tau_{xy} \\ \tau_{yy} \\ u\tau_{xy} + v\tau_{yy} - q_y \end{bmatrix}$$

The scalars q_x and q_y are the Cartesian components of the heat flux vector $\underline{q} = -k\nabla T$, where k is the thermal conductivity, and T is the static temperature. The scalars τ_{xx}, τ_{xy} and τ_{yy} are the Cartesian components of the stress tensor $\underline{\underline{\tau}}$. Such tensor depends on the divergence of the flow velocity vector $\underline{v}$, and the strain tensor $\underline{\underline{s}} = (\nabla v + \nabla v^T)/2$. For a Newtonian fluid one has $\underline{\underline{\tau}} = 2\mu[\underline{\underline{s}} - 1/3(\nabla \cdot v)I]$, where μ is the dynamic viscosity.

Harmonic balance formulation

The HB formulation of the NS equations assumes that the fundamental frequency ω of the sought periodic flow field is known. Denoting by $\mathbf{u}$ and $\mathbf{h}$ respectively the volume and surface integral of Eqn. (1), one can approximate both variables by means of the following truncated Fourier series, in which the retained number of harmonics N_H is a user-given parameter:

$$\mathbf{u}(t) \approx \hat{\mathbf{u}}_0 + \sum_{l=1}^{N_H} \left(\hat{\mathbf{u}}_{2l-1} \cos(l\omega t) + \hat{\mathbf{u}}_{2l} \sin(l\omega t) \right) \tag{4}$$

$$\mathbf{h}(t) \approx \hat{\mathbf{h}}_0 + \sum_{l=1}^{N_H} \left(\hat{\mathbf{h}}_{2l-1} \cos(l\omega t) + \hat{\mathbf{h}}_{2l} \sin(l\omega t) \right) \tag{5}$$

Inserting expansions (4) and (5) into Eqn. (1), and 'balancing' or matching harmonics of the same order results in a system of $[N_{pde} \times (2N_H + 1)]$ PDE's, the matrix-vector form of which is:

$$\omega A \hat{\mathbf{u}} + \hat{\mathbf{h}} = 0 \tag{6}$$

Here $\hat{\mathbf{u}} = [\hat{\mathbf{u}}_0' \ \hat{\mathbf{u}}_1' \dots \hat{\mathbf{u}}_{2N_H}']'$, $\hat{\mathbf{h}} = [\hat{\mathbf{h}}_0' \ \hat{\mathbf{h}}_1' \dots \hat{\mathbf{h}}_{2N_H}']'$, and matrix A is defined as:

$$
A = \begin{bmatrix} 0 & 0 & 0 & \cdots & 0 \\ 0 & J_1 & 0 & \cdots & 0 \\ 0 & 0 & J_2 & \cdots & 0 \\ \cdots & \cdots & \cdots & \cdots & \cdots \\ 0 & 0 & 0 & \dots & J_{N_H} \end{bmatrix}
\qquad
\begin{array}{c} J_l = I_{N_{eqs}} \otimes l \begin{bmatrix} 0 & 1 \\ -1 & 0 \end{bmatrix} \\[2em] l = 1, 2, \cdots, N_H \end{array}
\tag{7}
$$

where the symbol $\otimes$ detones the Kronecker tensor product, $I_{N_{eqs}}$ denotes the identity matrix of size $(N_{eqs})^2$, $N_{eqs} = N_{pde}$, and blocks J_l have size $(2N_{pde})^2$. Writing explicitly the equations of system (6), one finds that the unknown harmonic components $\hat{\mathbf{u}}$ are coupled by the harmonic residuals $\hat{\mathbf{h}}$, whereas no coupling occurs through the first term of the equation, since matrix A is block diagonal. As pointed out in [6], however, the computational cost of the HB system (6) grows cubically with the number of retained harmonics N_H, and the analytical derivation of the equations becomes extremely complex when dealing with the turbulence models required for high Reynolds number flows.

To alleviate these problems, it has been noted that an alternative formulation of the HB equations is obtained by reconstructing the Fourier coefficients of the volume integral $\hat{\mathbf{u}}$ of the conservation variables and the surface integral $\hat{\mathbf{h}}$ of the fluxes from the knowledge of the temporal behavior of $\mathbf{u}(t)$ and $\mathbf{h}(t)$ at $2N_H + 1$ equally spaced points over one period. Such points are defined by:

$$
t_n = \frac{n}{(2N_H + 1)} \frac{2\pi}{\omega}, \qquad n = 0, 1, \cdots, 2N_H
\tag{8}
$$

Let $\tilde{\mathbf{u}} = [\tilde{\mathbf{u}}_0' \ \tilde{\mathbf{u}}_1' \dots \tilde{\mathbf{u}}_{2N_H}']' = [\mathbf{u}(t_0)' \ \mathbf{u}(t_1)' \dots \mathbf{u}(t_{2N_H})']'$ and $\tilde{\mathbf{h}} = [\tilde{\mathbf{h}}_0' \ \tilde{\mathbf{h}}_1' \dots \tilde{\mathbf{h}}_{2N_H}']' = [\mathbf{h}(t_0)' \ \mathbf{h}(t_1)' \dots \mathbf{h}(t_{2N_H})']'$. In view of these definitions, expansions (4) and (5) yield:

$$
\tilde{\mathbf{u}} = F_H^{-1} \hat{\mathbf{u}} \quad \text{and} \quad \tilde{\mathbf{h}} = F_H^{-1} \hat{\mathbf{h}}
\tag{9}
$$

with $F_H = E_H \otimes I_{N_{pde}}$ and the Fourier matrix E_H^{-1} given by:

$$
\begin{bmatrix}
1 & \cos(\omega t_0) & \sin(\omega t_0) & \cdots & \cos(N_H \omega t_0) & \sin(N_H \omega t_0) \\
1 & \cos(\omega t_1) & \sin(\omega t_1) & \cdots & \cos(N_H \omega t_1) & \sin(N_H \omega t_1) \\
\cdots & \cdots & \cdots & \cdots & \cdots & \cdots \\
1 & \cos(\omega t_{2N_H}) & \sin(\omega t_{2N_H}) & \cdots & \cos(N_H \omega t_{2N_H}) & \sin(N_H \omega t_{2N_H})
\end{bmatrix}
$$

Computing the inverse of relationships (9), inserting these latter into Eqn. (6), and premultiplying Eqn. (6) by F_H^{-1} yields the system:

$$
\omega D \tilde{\mathbf{u}} + \tilde{\mathbf{h}} = 0
\tag{10}
$$

in which

$$D = F_H^{-1} A F_H \qquad (11)$$

Inserting the integral definitions of **u** and **h** into Eqn. (10) leads to the so called *high-dimensional harmonic balance formulation* [19] of the NS equations:

$$\omega D \left(\int_{C_H(t)} \mathbf{U}_H \, dC_H \right) + \oint_{S_H(t)} (\underline{\Phi}_{i,H} - \underline{\Phi}_{v,H}) \cdot d\underline{S}_H = 0 \qquad (12)$$

where $\mathbf{U}_H = [\mathbf{U}(t_0)' \; \mathbf{U}(t_1)' \ldots \mathbf{U}(t_{N_H})']'$, $\Phi_{i/v,H} = [\Phi_{i/v}(t_0)' \; \Phi_{i/v}(t_1)' \ldots \Phi_{i/v}(t_{N_H})']'$, and similar expressions hold for C_H and S_H. Moving from the time- to the frequency-domain, the number of PDE's increases from N_{pde} to $[N_{pde} \times (2N_H + 1)]$. Despite the fact that the number of PDE's to be solved has increased, the HB approach allows one to compute unsteady periodic flows at a substabtially lower computational cost with respect to the time-domain approach.

CFD SOLVER

Space discretization

The structured multi-block finite volume cell-centered parallel CFD code *COSA* [18, 20, 21] solves the integral form of both the TD conservation laws (system (1)) and the HB conservation laws (system (12)) making use of a second order upwind scheme. The discretization of the convective fluxes is based on Van Leer's *MUSCL* extrapolations and Roe's flux-difference splitting. Denoting by $\underline{n}$ the normal of the face of a grid cell, and dS the area of such face, the numerical approximation to the continuous convective flux component $\Phi_{i,f} = (\underline{\Phi}_i \cdot \underline{n}) dS$ through such face is:

$$\Phi_{i,f}^* = \frac{1}{2} \left[\Phi_{i,f}(\mathbf{U}_L) + \Phi_{i,f}(\mathbf{U}_R) - \left| \frac{\partial \Phi_{i,f}}{\partial \mathbf{U}} \right| \delta \mathbf{U} \right] \qquad (13)$$

Here the superscript *, the subscript $_f$, and the subscripts $_L$ and $_R$ denote numerical approximation, face value, and value extrapolated from the left and from the right, respectively. The numerical dissipation depends on the generalized flux Jacobian $\partial \Phi_{i,f} / \partial \mathbf{U}$ and the flow state discontinuity across the cell face, defined by $\delta U = (\mathbf{U}_R - \mathbf{U}_L)$.

The discretization of the viscous fluxes is based on second order centered finite-differences. The Cartesian derivatives of the flow velocity components are computed with the chain rule, using the derivatives of such components with respect to the local generalized curvilinear coordinates associated with the grid lines, and the grid metrics.

Integration of time-domain equations

The physical time-derivative of system (1) is discretized with a second-order backward finite-difference. The set of nonlinear algebraic equations resulting from the space- and time-discretization of system (1) is then solved with an explicit approach based on

the use of a fictitiuos time-derivative (Jameson's dual-time- stepping [22]). The discretization of the physical time- derivative of the unknown flow state by means of a second order backward finite difference, and the introduction of the derivative with respect to the fictitious time τ yield the equation:

$$V\frac{d\mathbf{Q}^{n+1}}{d\tau} + \mathbf{R}_g(\mathbf{Q}^{n+1}) = 0 \tag{14}$$

where

$$\mathbf{R}_g(\mathbf{Q}^{n+1}) = \frac{3\mathbf{Q}^{n+1} - 4\mathbf{Q}^n + \mathbf{Q}^{n-1}}{2\Delta t}V + \mathbf{R}_\Phi(\mathbf{Q}^{n+1}) \tag{15}$$

The entries of the array $\mathbf{Q}$ are the unknown flow variables at the N_{cell} cells discretizing the computational domain. The array $\mathbf{Q}$ can be viewed as made up of N_{cell} subarrays, each of which stores the N_{pde} flow unknowns at a particular physical time. The length of $\mathbf{Q}$ is therefore $(N_{pde} \times N_{cell})$. The array $\mathbf{R}_\Phi$ stores the cell residuals, and its structure is the same as that of $\mathbf{Q}$. For each cell, the N_{pde} residuals are obtained by adding the convective fluxes $\Phi^*_{i,f}$ and the viscous fluxes $\Phi^*_{v,f}$ through all the faces of the cell. The symbol $\mathbf{R}_g$ denotes instead a residual vector which also includes the source terms associated with the discretization of physical time-derivative $\partial \mathbf{U}/\partial t$ contained in Eqn. (1). The diagonal matrix V stores the volumes of the grid cells. It can be viewed as a block-diagonal matrix of size $(N_{cell} \times N_{cell})$ with each block being the identity matrix of size $(N_{pde} \times N_{pde})$ multiplied by the volume of the cell the block refers to. Note that V is independent of the physical time-level (denoted by the superscripts $n+1$, n and $n-1$) because in this report only rigid-body grid motion is considered. The symbol Δt indicates the user-given physical time-step. Equation (14) can thus be viewed as a system of $(N_{pde} \times N_{cell})$ ordinary differential equations (ODE's) in which the unknown is $\mathbf{Q}^{n+1}$, the flow state at time-level $n+1$. The calculation of $\mathbf{Q}^{n+1}$ is performed iteratively by discretizing the fictitious time-derivative $(d\mathbf{Q}^{n+1}/d\tau)$ of Eqn. (14) with a four-stage Runge-Kutta (RK) scheme, and marching the equations in pseudo-time until a steady state is achieved. Such steady state is the flow solution for the physical time being considered. The convergence rate is then greatly enhanced by means of local time-stepping (LTS), variable-coefficient central *implicit residual smoothing* (IRS) and a *full-approximation scheme* multigrid (MG) algorithm.

This solution procedure may become unstable when the physical time-step Δt is significantly smaller than the pseudo-time-step $\Delta \tau$. This instability was reported in [23],and thoroughly investigated by Melson *et al.* [24]. The latter study elegantly solved the stability problem by treating implicitly the $\mathbf{Q}^{n+1}$ term of the physical time-derivative within the RK integration process. This strategy has also been implemented in COSA, as summarized below. The residual $\mathbf{R}_g$ is split into the contribution depending on the $\mathbf{Q}^{n+1}$ term of the physical time- derivative, and a term $\mathbf{R}_d$ equal to the difference of $\mathbf{R}_g$ and the aforesaid $\mathbf{Q}^{n+1}$ term:

$$\mathbf{R}_g(\mathbf{Q}^{n+1}) = \frac{V}{\Delta t}\left[\frac{3}{2}\mathbf{Q}^{n+1} + g(\mathbf{Q}^n, \mathbf{Q}^{n-1})\right] + \mathbf{R}_\Phi(\mathbf{Q}^{n+1})$$

where $g(\mathbf{Q}^n, \mathbf{Q}^{n-1}) = -2\mathbf{Q}^n + 0.5\mathbf{Q}^{n-1}$. This equation can also be written as:

$$\mathbf{R}_g(\mathbf{Q}^{n+1}) = \mathbf{R}_d(\mathbf{Q}^{n+1}) + \frac{3V}{2\Delta t}\mathbf{Q}^{n+1} \tag{16}$$

TURBO-10-1073, M.S. Campobasso

Discretising the fictitious time-derivative of Eqn. (14) with a multi-stage RK scheme, introducing the decomposition of $\mathbf{R}_g$ provided by Eqn. (16), and considering the $\mathbf{Q}^{n+1}$ term at stage k rather than at stage $(k-1)$ yields the following modified RK algorithm:

$$
\begin{aligned}
\mathbf{W}^0 &= \mathbf{Q}_l \\
(I + \alpha_k \beta)\mathbf{W}^k &= \mathbf{W}^0 - \alpha_k \Delta\tau V^{-1} \mathbf{R}_d(\mathbf{W}^{k-1}) \\
\mathbf{Q}_{l+1} &= \mathbf{W}^{NS}
\end{aligned}
\tag{17}
$$

where k varies between 1 and the number of RK stages NS, α_k is the kth RK coefficient, $\beta = 1.5\Delta\tau/\Delta t$, l is the RK cycle counter, and $\mathbf{Q}_l$ is shorthand for $\mathbf{Q}_l^{n+1}$. The stability analysis of [24] shows that the stability of algorithm (17) no longer depends on the ratio $\Delta\tau/\Delta t$. However this formulation is still unsuitable when IRS and MG are also used, because both acceleration techniques have to be applied to a residual term that vanishes at convergence, and this is not the case of $\mathbf{R}_d$. The solution is to introduce the residual $\mathbf{R}_g$ which does vanish at convergence. Given that:

$$
\Delta\tau \mathbf{R}_d(\mathbf{W}) = -\beta V \mathbf{W} + \Delta\tau \mathbf{R}_g(\mathbf{W})
$$

the IRS-MG-tailored counterpart of algorithm (17) is:

$$
\begin{aligned}
\mathbf{W}^0 &= \mathbf{Q}_l \\
(I + \alpha_k \beta)\mathbf{W}^k &= \mathbf{W}^0 + \alpha_k \beta \mathbf{W}^{k-1} \\
&\quad - \alpha_k \Delta\tau V^{-1} L_{IRS}[\mathbf{R}_g(\mathbf{W}^{k-1}) + \mathbf{f}_{MG}] \\
\mathbf{Q}_{l+1} &= \mathbf{W}^{NS}
\end{aligned}
\tag{18}
$$

where L_{IRS} denotes the IRS operator, and $\mathbf{f}_{MG}$ is the MG forcing function, which is nonzero when the smoother (18) is used on a coarse level after a restriction step [25]. Note that the matrix multiplying $\mathbf{W}^k$ at the second line of algorithm (18) is diagonal, and this implies that for each grid cell the N_{pde} unknowns can be updated without an actual matrix inversion.

Integration of harmonic balance equations

At the differential level, the only difference between system (1) and system (12) is that the physical time-derivative of the former system is replaced by a volumetric source term proportional to ω in the latter. The set of nonlinear algebraic equations resulting from the space-discretization of system (12) is thus solved with the same technique used for steady problems [20], namely the four-stage RK smoother accelerated by LTS, IRS and MG. The introduction of the derivative with respect to the fictitious time τ yields the equation:

$$
V_H \frac{d\mathbf{Q}_H}{d\tau} + \mathbf{R}_{g,H}(\mathbf{Q}_H) = 0
\tag{19}
$$

where

$$\mathbf{R}_{g,H}(\mathbf{Q}_H) = \omega V_H D \mathbf{Q}_H + \mathbf{R}_{\Phi,H}(\mathbf{Q}_H) \tag{20}$$

The array $\mathbf{Q}_H$ is made up of $(2N_H + 1)$ flow states referring to the physical times defined by Eqn. (8). Therefore, one has $\mathbf{Q}_H = [\mathbf{Q}_0' \ \mathbf{Q}_1' \dots \mathbf{Q}_{2N_H}']' = [\mathbf{Q}(t_0)' \ \mathbf{Q}(t_1)' \dots \mathbf{Q}(t_{2N_H})']'$, and each subarray of $\mathbf{Q}_H$ has length $(N_{pde} \times N_{cell})$. The arrays $\mathbf{R}_{g,H}$ and $\mathbf{R}_{\Phi,H}$ have the same structure of $\mathbf{Q}_H$. The subarray $(\mathbf{R}_\Phi)_n$ $(n = 0, 1, \cdots, 2N_H)$ denotes the grid-residuals associated with the convective and viscous fluxes at time t_n. The subarray $(\mathbf{R}_g)_n$ denotes instead a residual vector which also includes the source term $\omega V_H D \mathbf{Q}_H$. The diagonal matrix V_H is given by $V_H = I_{2N_H+1} \otimes V$. Matrix D is defined by Eqn. (11), and the matrix A appearing herein is defined by Eqn. (7) where $N_{eqs} = N_{pde} \times N_{cell}$.

Equation (19) can thus be viewed as a system of $[N_{pde} \times N_{cell} \times (2N_H + 1)]$ ODE's in the unknown $\mathbf{Q}_H$. The calculation of $\mathbf{Q}_H$ is performed iteratively by discretizing the fictitious time-derivative $(d\mathbf{Q}_H/d\tau)$ of Eqn. (19) with a four-stage RK scheme, and marching the equations in pseudo-time until a steady state is achieved. The IRS and the MG acceleration techniques are also used exactly as for steady and TD problems.

Although no rigorous stability analysis has been carried out yet, the authors have found that this explicit MG solution procedure of the HB equations may become numerically unstable for certain type of aerodynamic problems. More specifically, a numerical instability of the HB MG iteration has been encountered in the solution of the transonic flow problems with the COSA solver reported in [9]. It is the authors' view that this instability is the FD counterpart of the TD one, discussed in the preceding subsection. In the TD framework, the instability may occur when the physical time-step Δt is significantly smaller than the pseudo-time step $\Delta \tau$. With transonic flows, for example, this may occur in the supersonic region upstream of a shock. In the HB context, the equivalent physical time-step Δt is given by $\Delta t = 2\pi/\omega/(2N_H + 1)$. In order to stabilize the RK-IRS-MG iteration used to solve the HB equations for all flow regimes, a stabilization procedure similar to that proposed by [24] has been successfully implemented and tested in the COSA solver. To the best of the authors' knowledge, this is the first reported study on the use of this method for the solution of the HB Euler and NS equations. The stability problem is removed by treating implicitly the source term of Eqn. (20) within the RK integration process. Discretising the fictitious time-derivative of Eqn. (19) with a multi-stage RK scheme, and considering the source term of Eqn. (20) at stage k rather than at stage $(k-1)$ yields the following modified RK algorithm:

$$\begin{aligned}
\mathbf{W}_H^0 &= (\mathbf{Q}_H)_l \\
(I + \alpha_k \beta_H D)\mathbf{W}_H^k &= \mathbf{W}_H^0 - \alpha_k \Delta \tau V_H^{-1} \mathbf{R}_{\Phi,H}(\mathbf{W}_H^{k-1}) \\
(\mathbf{Q}_H)_{l+1} &= \mathbf{W}_H^{NS}
\end{aligned} \tag{21}$$

where $\beta_H = \omega \Delta \tau$ and the other symbols have been defined in the preceding subsection. This formulation is still unsuitable when IRS and MG are also used, because both acceleration techniques have to be applied to a residual term that vanishes at convergence, and this is not the case of $\mathbf{R}_{\Phi,H}$. The solution is to introduce the residual $\mathbf{R}_{g,H}$ which instead vanishes at convergence. The IRS-MG-tailored

counterpart of algorithm (21) is:

$$
\begin{aligned}
\mathbf{W}_H^0 &= (\mathbf{Q}_H)_l \\
(I + \alpha_k \beta_H D)\mathbf{W}_H^k &= \mathbf{W}_H^0 + \alpha_k \beta_H D \mathbf{W}_H^{k-1} \\
&\quad - \alpha_k \Delta \tau V_H^{-1} L_{IRS,H}[\mathbf{R}_{g,H}(\mathbf{W}_H^{k-1}) + \mathbf{f}_{MG,H}] \\
(\mathbf{Q}_H)_{l+1} &= \mathbf{W}_H^{NS}
\end{aligned}
\tag{22}
$$

where the HB MG forcing function is defined as $\mathbf{f}_{MG,H} = [\mathbf{f}_{MG}(t_0)' \ \mathbf{f}_{MG}(t_1)' \ldots \mathbf{f}_{MG}(t_{2N_H})']'$ with the $(2N_H + 1)$ values of t_n defined by Eqn. (8), and the HB IRS operator $L_{IRS,H}$ can be viewed as a $[(2N_H + 1) \times (2N_H + 1)]$ block-diagonal matrix, the nonzero blocks of which are the $(2N_H + 1)$ $L_{IRS}(t_n)$ operators. Note that the matrix multiplying $\mathbf{W}_H^k$ at the second line of algorithm (22) is not diagonal. For each grid cell, the update of the $[N_{pde} \times (2N_H + 1)]$ unknowns requires the inversion of one $[(2N_H + 1) \times (2N_H + 1)]$-sub-block of $(I + \alpha_k \beta_H D)$. Such overhead results in the computational cost of the HB analysis growing in a moderately superlinear fashion with respect to N_H. Despite this feature, however, the computational cost of the HB analysis remains competitive with that of the TD analysis. As an example, the transonic flow studies performed with the COSA solver based on algorithm (22) and reported in [9] show that the HB analysis can predict the periodic body forces acting on a pitching airfoil with extremely small errors with respect to the TD analysis, but requiring a CPU-time about one order of magnitude smaller. These HB transonic flow analyses failed to converge when the standard rather than the stabilized RK algorithm (22) was used.

It has been observed that the use of an explicit approach to integrate the HB NS equations requires the introduction of an additional constraint on the size of the local time-step used to pseudo-time-march the solution for stability reasons [8]. Such constraint depends on the fundamental frequency ω and the number of complex harmonics N_H, and becomes more stringent as either parameter increases. In this circumstance, the number of MG iterations required for convergence would increase as N_H increases. The use of the stabilization presented herein, on the other hand, removes this additional constraint, thus making the convergence rate more independent of N_H. When using an explicit integration method, however, the convergence rate of explicit HB solvers may still show a certain degree of dependence on N_H for flow problems with significant nonlinearities. This is because one of the factors on which the convergence rate of iterative solvers depends is the features of the overall Jacobian (*e.g.* condition number, degree of non-normality and diagonal dominance) of the HB NS equations, made up of the sum of the standard flux Jacobian of the steady NS equations and the term $\omega V_H D$. The last term is an antisymmetric matrix, the size and magnitude of which grow with N_H and ω respectively. Its main effect is to reduce the diagonal dominance and increase the non-normality of the HB Jacobian with respect to that of the Jacobian of the steady equations. A reduction of the diagonal dominance impairs the convergence rate of iterative stationary linear smoothers such as the Gauss-Seidel and the symmetric successive over-relaxation iterations. The effect of N_H and ω on the diagonal dominance of the HB Jacobian of the HB equations is analyzed in reference [7], which also uses a robust preconditioned Krylov subspace solver to greatly reduce the dependence of the computational cost of an implicit HB solver on these two parameters. A significant level of non-normality of the HB Jacobian may result in numerical transients during which significant reductions of the convergence properties of linear smoothers (including the RK

iteration) with respect to the theoretical expectation are experienced [26]. These observations refer to the case in which the standard non-stabilized integration of the HB equations is used. When the stabilized integration is used, however, the non-normality characteristics of the linear operator corresonding to the iteration (22) may differ from those of the standard HB Jacobian. This mathematical aspect is still under investigation. For these reasons, it is expected that the convergence rate of the presented MG HB solver will be fairly close to that of the associated steady problem, and independent of N_H for problems with low level of flow nonlinearity. For problems with significant nonlinearities, however, the convergence rate of the HB solver may worsen with respect to that of the steady state when N_H is increased because of the significant contribution of the higher harmonics to the non-normality of the overall HB Jacobian.

When solving the HB equations with an implicit approach, the HB source term has to be treated implicitly for stability reasons [10, 11]. This constraint may require substantial code extensions if the HB solver is built around an existing code. It may also yield very large memory usage for storing the Jacobian associated with all $(2N_H + 1)$ flow states if a Krylov-subspace method with approximate Jacobian-based preconditioning is used for the solution of the linear systems arising at each step of Newton's method. One possible solution is to use an iterative stationary linear block-solver such as block-Jacobi to solve the linear systems, as this allows one to treat separately the Jacobians associated with each flow snapshot during the integration [10]. An alternative solution to simplify the development of the HB technology around an existing implicit solver is the treatment of the HB source term presented in [27].

LOW-SPEED PRECONDITIONING

In the case of low-speed flows, a large disparity between the convective and acoustic eigenvalues of the flux Jacobian $\partial \Phi_{i,f}/\partial \mathbf{U}$ exists. This results in unbalanced amounts of numerical dissipation, and this occurrence spoils the accuracy of the solution. When using explicit time-marching methods, the local time-step also depends on the eigenvalues of the flux Jacobian, and a large disparity between convective and acoustic speeds substantially impairs the convergence rate of the solver. These problems are circumvented by using low-speed preconditioning [17].

In the case of time-dependent problems, the pseudo-time derivative of Eqn. (14) is premultiplied by a preconditioning matrix $(\Gamma_c)^{-1}$. This results in a rescaling of the eigenvalues of the flux Jacobian which restores the correct levels of numerical dissipation and allows one to maintain high convergence rates even with low-speed problems. The preconditioner Γ_c used by COSA is that proposed in [17], where its expression can be found. The matrix Γ_c depends on a parameter M_p. The choice $M_p = 1$ yields no preconditioning. For low-speed flows, the parameter M_p is:

$$M_p = \min\left(\max\left(M, M_{pg}, M_{vis}, M_{uns}, \varepsilon\right), 1\right) \tag{23}$$

where M is the actual local Mach number, M_{pg} is a cut-off value based on the local pressure gradient [28, 29], M_{vis} is a cut-off value based on the cell Reynolds number (also called Peclet number) [30], M_{uns} is a cut-off value based on the physical time-step Δt and the characteristic lengths of the domain [17], and ε is a small cut-off parameter that prevents the preconditioner from becoming singular at stagnation points.

The introduction of preconditioning modifies the artificial dissipation term of the numerical flux provided by Eqn. (13) as follows:

$$\Phi_{i,f}^* = \frac{1}{2}\left[\Phi_{i,f}(\mathbf{U}_L) + \Phi_{i,f}(\mathbf{U}_R) - \Gamma_c^{-1}\left|\Gamma_c\frac{\partial\Phi_{i,f}}{\partial\mathbf{U}}\right|\delta\mathbf{U}\right] \tag{24}$$

For steady problems, the choice of Eqn. (23) with $M_{uns} = 0$ to build Γ_c and its inverse guarantees both the balance of the numerical dissipation and an optimal convergence rate. For time-dependent problems, however, the use of Eqn. (23) with M_{uns} defined as proposed in [17] usually yields a high convergence rate, but does not guarantee an optimal scaling of the artificial dissipation. This has been observed by the same developers of this preconditioner for time-dependent problems with motionless grids [31], and more recently confirmed by the authors of this paper for the case of time-dependent problems with moving grids [18]. The latter article also presented a *mixed preconditioning* strategy to overcome this problem, and demonstrated its effectiveness with a number of time-dependent problems with motionless and moving grids. In essence, mixed preconditioning consists of using the steady preconditioning parameter (*i.e.* the value of M_p obtained from Eqn. (23) after setting $M_{uns} = 0$) to construct the preconditioner required to calculate the numerical dissipation, and the unsteady preconditioning (*i.e.* the complete form of Eqn. (23)) to construct the preconditioner needed to compute the preconditioned eigenvalues used in the calculation of the local time-step. The modified numerical flux is thus:

$$\Phi_{i,f}^* = \frac{1}{2}\left[\Phi_{i,f}(\mathbf{U}_L) + \Phi_{i,f}(\mathbf{U}_R) - \Gamma_{cu}^{-1}\left|\Gamma_{cs}\frac{\partial\Phi_{i,f}}{\partial\mathbf{U}}\right|\delta\mathbf{U}\right] \tag{25}$$

where the subscripts $_{cs}$ and $_{cu}$ respectively denote the use of the steady and unsteady preconditioning parameters to build the preconditioner Γ_c.

The general form of the standard TD RK-IRS-MG iteration featuring LSP, obtained by premultiplying the fictitious time-derivative of Eqn.(14) by Γ_{cu}^{-1}, and discretizing this derivative with the multistage RK of choice, is:

$$\begin{aligned}
\mathbf{W}^0 &= \mathbf{Q}_l \\
\mathbf{W}^k &= \mathbf{W}^0 \\
&\quad -\alpha_k\Delta\tau V^{-1}L_{IRS}\Gamma_{cu}[\mathbf{R}_g(\mathbf{W}^{k-1}) + \mathbf{f}_{MG}] \\
\mathbf{Q}_{l+1} &= \mathbf{W}^{NS}
\end{aligned} \tag{26}$$

The use of the stabilization process of the RK cycle discussed in the previous subsections yields the following stabilized iteration:

$$\begin{aligned}
\mathbf{W}^0 &= \mathbf{Q}_l \\
(I + \alpha_k\beta\Gamma_{cu}^{k-1})\mathbf{W}^k &= \mathbf{W}^0 + \alpha_k\beta\Gamma_{cu}^{k-1}\mathbf{W}^{k-1} \\
&\quad -\alpha_k\Delta\tau V^{-1}L_{IRS}\Gamma_{cu}^{k-1}[\mathbf{R}_g(\mathbf{W}^{k-1}) + \mathbf{f}_{MG}] \\
\mathbf{Q}_{l+1} &= \mathbf{W}^{NS}
\end{aligned} \tag{27}$$

The matrix premultiplying $\mathbf{W}^k$ is block-diagonal, but its blocks are not diagonal because of the preconditioner Γ_{cu} which is not a diagonal operator. Therefore the update process requires the inversion of an $(N_{pde} \times N_{pde})$-matrix for each cell of the computational domain. The interested reader is referred to [18] for further details on the LSP implementation of the COSA solver.

In the case of frequency-domain problems, the pseudo-time derivative of Eqn. (19) is premultiplied by a $[(2N_H + 1) \times (2N_H + 1)]$-block-matrix $\Gamma_{c,H}^{-1}$, and the nonzero blocks $\Gamma_{c,n}^{-1}$ with $n = 0, 1, \cdots, 2N_H$ are simply instantiations of the preconditioning matrix Γ_c^{-1} discussed above at the times defined by Eqn. (8). In all the HB analyses reported in the remainder of this paper, the steady preconditioner set up (*i.e.* a value of M_p obtained by setting $M_{uns} = 0$ in Eqn. (23)) has been used for the calculation of both the numerical dissipation and the local time-step. The general form of the standard HB RK-IRS-MG iteration featuring LSP is:

$$
\begin{aligned}
\mathbf{W}_H^0 &= (\mathbf{Q}_H)_l \\
\mathbf{W}_H^k &= \mathbf{W}_H^0 \\
&\quad - \alpha_k \Delta \tau V_H^{-1} L_{IRS,H} \Gamma_{c,H} [\mathbf{R}_{g,H}(\mathbf{W}_H^{k-1}) + \mathbf{f}_{MG,H}] \\
(\mathbf{Q}_H)_{l+1} &= \mathbf{W}_H^{NS}
\end{aligned}
\tag{28}
$$

The use of the stabilization process of the RK cycle discussed in the previous subsections yields the following stabilized iteration:

$$
\begin{aligned}
\mathbf{W}_H^0 &= (\mathbf{Q}_H)_l \\
(I + \alpha_k \beta_H \Gamma_{c,H}^{k-1} D) \mathbf{W}_H^k &= \mathbf{W}_H^0 + \alpha_k \beta_H \Gamma_{c,H}^{k-1} D \mathbf{W}_H^{k-1} - \alpha_k \Delta \tau V_H^{-1} \\
&\quad L_{IRS,H} \Gamma_{c,H}^{k-1} [\mathbf{R}_{g,H}(\mathbf{W}_H^{k-1}) + \mathbf{f}_{MG,H}] \\
(\mathbf{Q}_H)_{l+1} &= \mathbf{W}_H^{NS}
\end{aligned}
\tag{29}
$$

The matrix premultiplying $\mathbf{W}_H^k$ is block-diagonal, but its blocks are not diagonal because both the preconditioner Γ_c and the matrix D are not diagonal. Each of these N_{cell} blocks has size $[(2N_H + 1) \times N_{pde}]^2$, and the update process of the whole solution requires the inversion of all such blocks. Due to this feature, the computational cost of HB analyses is moderately superlinear with respect to N_H. All numerical analyses carried out thus far, however, show that the computational speed of the HB analysis remains significantly higher than that of the TD despite the abovesaid overhead.

TWO-DIMENSIONAL YAWED WIND MODELING

In order to define boundary data and motion parameters for the 2D TD and FD analyses presented in the result section, the unsteady flow regime experienced by the airfoils of a HAWT blade in yawed wind has to be defined as a function of the freestream wind speed $\underline{V}_{fs}$, the turbine rotational speed $\underline{\omega}$, the angle δ between $\underline{V}_{fs}$ and the normal to the rotor plane (*yaw angle*), the chord c of the airfoil and its distance R from the rotational axis. The left and right plots of Fig. 1 respectively depict the top and front views of a HAWT in yawed wind, and highlight some of the aforementioned parameters. The circumferential position of a blade is defined by the angle θ, which is taken to be zero when the blade is vertical and descending (position *A*). The four plots of Fig. 2 report the velocity triangles associated
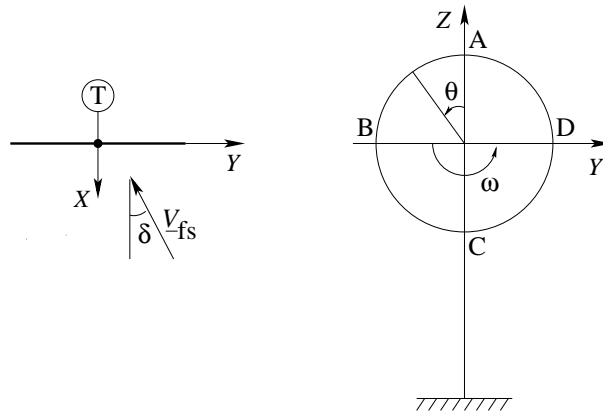
Figure 1. SCHEMATIC VIEWS OF HAWT IN YAWED WIND. LEFT PLOT: TOP VIEW; RIGHT PLOT: FRONT VIEW.

with a blade airfoil for the positions labeled A to D in the right plot of Fig. 1. The modulus of the axial velocity component is $|\underline{V}_{fs}|\cos(\delta)$, and is the same for all radial and circumferential positions. The modulus of the entrainment velocity $\underline{\omega} \times \underline{R}$ varies linearly with $|\underline{R}|$, and is therefore the same in all four triangles of Fig. 2. The velocity $\underline{W}_i$ and the angle α_i ($i = A, B, C, D$) denote respectively the freestream velocity and *inflow angle* observed by the blade section at radius $\underline{R}$, and both parameters vary with the circumferential position $\theta = \omega t$. Each velocity triangle is contained in the plane tangent to the cylinder of radius R centered on the rotational axis, and therefore it neglects any radial (*i.e.* along the blade axis) velocity component. The magnitude of the discarded radial component varies with θ: no component is discarded when the blade is vertical (positions A and C), as the entire vector $\underline{V}_{fs}$ is contained in the tangent plane; the entire radial component $\underline{V}_{fs}\sin(\delta)$ is instead neglected when the blade is horizontal (positions B and D), as the radial component of $\underline{V}_{fs}$ is orthogonal to the tangent plane. Within the limits of these approximations, the axial and circumferential components of the freestream velocity
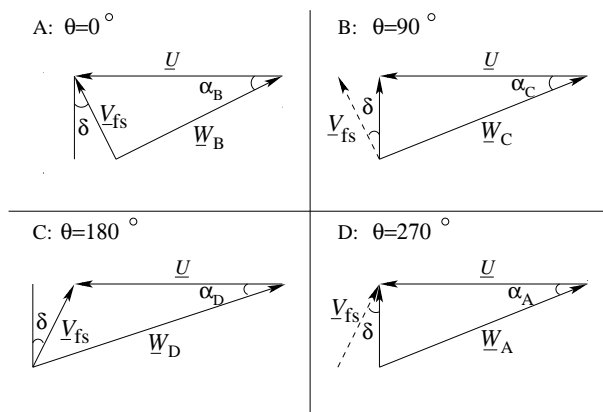
Figure 2. VELOCITY TRIANGLES OF HAWT BLADE SECTION FOR POSITIONS LABELED A TO D IN FIG. 1.

perceived by each blade section are respectively:

$$W_x = V_{fs}\cos(\delta) \tag{30}$$

$$W_\theta = \omega R - V_{fs}\sin(\delta)\cos(\omega t) \tag{31}$$

The 2D simulation of the unsteady flow past the blade airfoil of the HAWT in yawed wind could be performed by using a motionless domain and enforcing the time-dependent freestream velocity defined by conditions (30) and (31). Alternatively, one could also use a moving-domain simulation with steady farfield conditions and suitably defined grid motion. The modulus W_{fs} and the orientation α_{fs} of the uniform freestream are obtained by removing the time-dependent term of Eqn. (31), and their expressions are respectively:

$$W_{fs} = \sqrt{(V_{fs}\cos\delta)^2 + (\omega R)^2} \tag{32}$$

$$\alpha_{fs} = \arctan\left[(V_{fs}\cos\delta)/(\omega R)\right] \tag{33}$$

When using steady farfield boundary conditions, the variability of the inflow state associated with the case of motionless domain is equivalent to and can be replaced by a horizontal sinusoidal motion of the grid. The expression of such motion is:

$$\begin{aligned} h(t) &= h_0\sin(\omega t)\\ h_0 &= V_{fs}\sin\delta/\omega \end{aligned} \tag{34}$$

The moving domain model has been adopted for the analyses presented in the result section, and it could also be used to perform 2D experimental measurements aimed at studying the aerodynamic characteristics of HWAT airfoils in yawed wind. A typical HAWT airfoil twisted by an angle γ is depicted in the left plot of Fig. 3 along with an indication of the harmonic motion. The right plot provides a representation of Eqn. 34, and the four positions A to D correspond to those labeled with the same symbols in Figures 1 and 2.
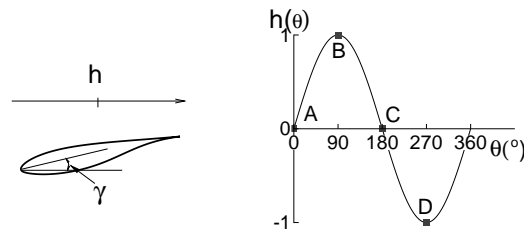

Figure 3.   HARMONIC MOTION OF HAWT BLADE SECTION CORRESPONDING TO YAWED INFLOW.

VALIDATION

The second order accuracy of the time-discretization for viscous flows has been verified by computing the unsteady laminar vortex shedding behind a cylinder. Several simulations have been performed, each of which has used a physical time-step obtained by halving that of the preceding simulation. The lift and drag forces obtained at a chosen time from each simulation have been used to perform Richardson's extrapolations, which have confirmed the second order accuracy of the time-discretization [32]. The second order accuracy of the convective flux discretization has been verified by computing the solution of a 2D inviscid test case for which the analytical solution has been determined. The problem has been solved using several grids, which become successively finer by a factor of two in both directions. Analysis of the RMS of the error between the analytical solution and the computed solutions obtained by using these grids have confirmed the second order of the space-discretization [20]. The second order accuracy of the time- and space-discretization of the solver using LSP has also been demonstrated by considering an unsteady test case resulting from the superposition of a uniform low-speed flow and a steady vortex. The analytical solution of this problem has been used to verify the second order accuracy of COSA for this type of problem [18].

To validate the implementation of the moving grid capabilities of the COSA solver, the unsteady flow field past a pitching flat plate has been considered. The time-dependent angular position of the flat plate varies accordind to $\Delta\theta_p \sin(\omega t)$, with $\Delta\theta_p$ positive in the clockwise direction. For the case in which the flat plate is aligned with a uniform stream when it takes its mean position ($\sin(\omega t) = 0$), an analytical solution of this problem has been provided by Theodorsen [33]. The input parameters of the analysis are $\Delta\theta_p$, the position of the hinge, the freestream velocity W_{fs}, and the reduced frequency λ, defined as:

$$\lambda = \omega c / W_{fs} \tag{35}$$

In the selected configuration, $\Delta\theta_p = 1^o$, the hinge is at 25 % chord from the leading edge, the freestream velocity corresponds to a Mach number of 0.001, and $\lambda = 0.1$. The TD analysis has been carried out using a 6-block grid with 129 points on each side of the flat plate, 97 points before the leading edge and after the trailing edge and 97 points in the normal direction. The freestream boundaries are placed at about 5 chords from the flat plate, and the minimum distance of the first grid points off the plate surface from the plate itself is 0.5 % of the chord. The period has been discretized with 32 intervals, and the simulation has been run for 2 periods. Figure 4 provides the theoretical prediction of the amplitude of the first harmonic of the differential static pressure coefficient c_p across the flat plate. The static pressure coefficient is defined as $c_p = (p - p_{fs})/0.5\rho_{fs}W_{fs}^2$, and the variable on the y-axis is the modulus of $\Delta c_p = c_{p,U} - c_{p,L}$, where the subscripts $_U$ and $_L$ denote upper and lower side respectively. The x-axis reports the position along the chord. Figure 4 also shows the profiles of $|\Delta c_p|$ computed by COSA with and without LSP. A very good agreement between the numerical result obtained with LSP and the theoretical prediction is observed. The bad agreement between theory and numerical prediction without LSP highlights the necessity of using LSP with low-speed flows to preserve numerical accuracy.
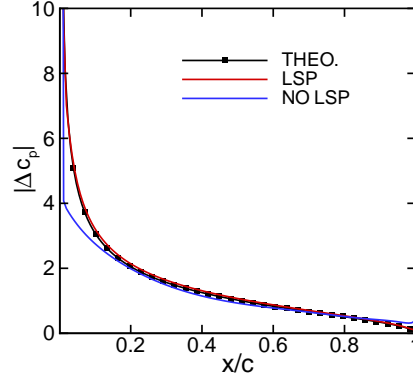
Figure 4. AMPLITUDE OF THE FIRST HARMONIC OF THE DIFFERENTIAL STATIC PRESSURE COEFFICIENT ACROSS A PITCHING FLAT PLATE: COMPARISON OF THEORETICAL RESULT AND NUMERICAL PREDICTIONS OBTAINED WITH AND WITHOUT LSP.

Table 1. INPUT PARAMETERS FOR THE 2D UNSTEADY MOVING-GRID CFD ANALYSES OF TWO SECTIONS OF HAWT BLADE.

section	M_{fs}	α_{fs} (^{o})	ϕ_{fs} (^{o})	h_0/c	λ
90 %	0.22	9.1	5.4	1.21	0.076
30 %	0.08	25.8	6.7	0.4	0.622

RESULTS

The 2D laminar flow field past two airfoils of a rotating HAWT blade in yawed wind is considered in this section. The blade height is 45.7 m and its rotational speed is 17.5 RPM, which corresponds to a value of ω of about 1.83 rad/s. The freestream wind velocity V_{fs} is 14 m/s, and a yaw angle δ of 30° is assumed. The sections at 90 and 30 percent blade height are considered. The former has a chord c of 3.16 m and a twist γ of 3.7^o; the chord and the twist of the latter are 9.48 m and 19.1^o respectively. Using the rotational speed ω, the chord and the relative freestream velocity defined by Eqn. (32), one can calculate the reduced frequency λ by means of Eqn. (35). The relative angle of attack (AoA) ϕ_{fs} is obtained by subtracting the twist γ to the inflow angle α_{fs} defined by Eqn. (33). Choosing a reference temperature of 288 K, one can calculate the Mach number M_{fs} corresponding to W_{fs}. The set of input data used for the 2D unsteady moving-grid simulations of the 2 sections is reported in Table 1. The airfoil selected for both sections is the NACA0012 airfoil, and the Reynolds number has been set to 1000. The C-grid adopted for all simulations has 321 points along the airfoil, 97 points in the grid cut, and 129 points in the normal-like direction. The farfield boundary is placed at about 20 chords from the airfoil, and the distance of the first grid points off the airfoil surface from the the surface itself is about 0.01 % of the chord. The airfoil and the whole grid are inclined by the twist angle γ on the horizontal direction. In the unsteady simulation, the whole grid undergoes a sinusoidal motion defined by Eqn. (34). All TD simulations have been performed using 128 time-intervals per period, and running the

TURBO-10-1073, M.S. Campobasso

simulations for 3 periods. The HB analyses for both sections have been performed for N_H varying between 1 and 5. The CFL number has been set to 3 for all simulations reported herein. Note that the choice of a relatively thin airfoil with respect to those typically used in HAWT's, and the lack of turbulence modeling, result in the unsteady flows analyzed in the next two subsections not being fully correspondent to those of real HAWT yawed conditions. The main objectives of the following analyses, however, are to a) assess the accuracy and the computational performance of the HB technology being developed against those of the conventional TD technology, and thus b) demonstrate the suitability of the HB technology with LSP for unsteady periodic flows with the same kinematic patterns of yawed HAWT flows.

Section at 90 % blade height

The lift coefficient c_l over one rotor revolution computed by the TD analysis and five HB analysis with $N_H = 1, \ldots 5$ is depicted in Fig. 5, the abscissa of which reports the percentage time of a period. The selected period of the TD simulation is the third one. These curves show that an accurate prediction of c_l by means of the HB analysis is achieved with $N_H \geq 2$. The plot also provides the value of the AoA ϕ_{fs} over the period, and it highlights that c_l increases as ϕ_{fs} decreases and viceversa. This happens because the flow on the upper side of the airfoil is separated at all times, and the reduction of the separation extent induced by a reduction of ϕ_{fs} causes c_l to increase. The hysteresis cycles of the lift coefficient, the drag coefficient c_d and the moment coefficient c_m are depicted in the three plots of Fig. 6, which confirms that the HB analyses with $N_H \geq 2$ lead to an excellent agreement with the TD result.
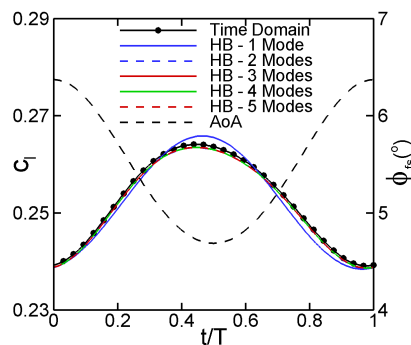
Figure 5. LIFT COEFFICIENT OF 90 % BLADE SECTION OVER ONE REVOLUTION COMPUTED WITH TD AND FIVE HB ANALYSES.

The real and imaginary part of the pressure coefficient c_p computed by the TD analysis and the 5 HB analyses are plotted in Figures 7-a and 7-b respectively. In both cases, the x-axis reports the position along the axial chord $c_{ax} = c \cos \gamma$. These figures also confirm that 2 harmonics are sufficient to resolve the flow unsteadiness with the HB analysis. The real and imaginary part of the absolute value of the skin-friction coefficient c_f computed by the TD analysis and the 5 HB analyses are instead plotted in Figures 8-a and 8-b respectively. In this case, one sees that an adequate HB resolution of the imaginary part of $|c_f|$ requires $N_H \geq 3$. Note that the sudden slope veering of both the real and imaginary parts of $|c_f|$ starting at about 60 % axial chord is due to the oscillation of the point where
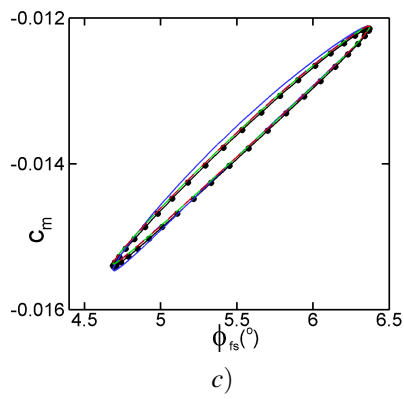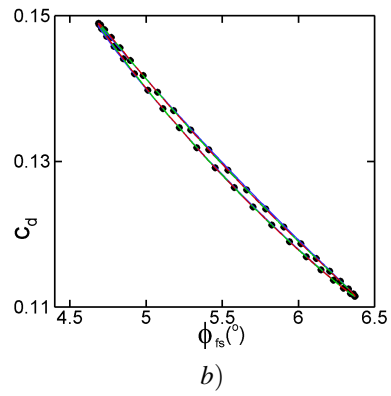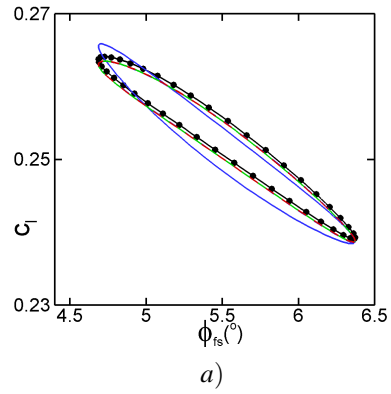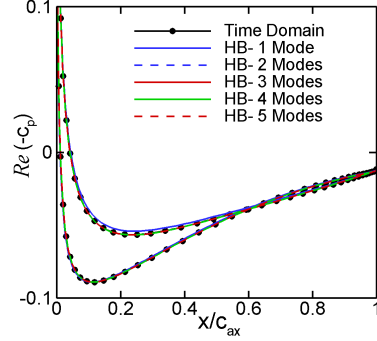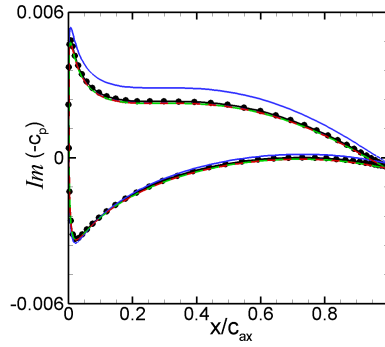
Figure 6.   HYSTERESIS FORCE LOOPS OF 90 % BLADE SECTION COMPUTED WITH TD AND FIVE HB ANALYSES (LINE LEGEND AS IN FIG. 5):
a) LIFT COEFFICIENT, b) DRAG COEFFICIENT, c) PITCHING MOMENT COEFFICIENT.

separation on the upper side of the airfoil occurs.

The convergence histories of the five HB analyses and that of the TD solver for a particular physical time are reported in Fig. 9.

Figure 7. PRESSURE COEFFICIENT OF 90 % BLADE SECTION COMPUTED WITH TD AND FIVE HB ANALYSES: a) REAL PART, b) IMAGINARY PART.

The variable on the x-axis is the number of multigrid iterations, and the variable l_r on the y-axis is the logarithm in base 10 of the RMS of all cell-residuals for all N_{pde} equations. The HB analyses have been run until $l_r \leq 1.d - 12$; the iterative solution process of each physical time-step of the TD analysis has been stopped either when $l_r \leq 1.d - 12$ or after 3000 MG iterations if at this stage this convergence tolerance had not been achieved. For most physical time-steps, however, the prescribed residual tolerance of $1.d - 12$ has been achieved well before the limit of 3000 MG iterations. An interesting feature is that the convergence histories of all HB analyses are practically superimposed, and thus independent of N_H. Figure 9 also reports the convergence history for the steady problem, which differs very little from that of the HB analyses. These convergence data point to the fact that the flow nonlinearity for this problem is fairly small, and therefore neither the contribution of the first harmonic to the HB source term nor that of the higher harmonics are sufficient to significantly affect the spectrum of the linearized operator associated with the integration of the HB equations with respect to that associated with the integration of the steady equations. All these analyses could be performed without the RK stabilization previously discussed, namely using algorithm (28) for the solution update. Therefore the cost of a single HB MG iteration is with good
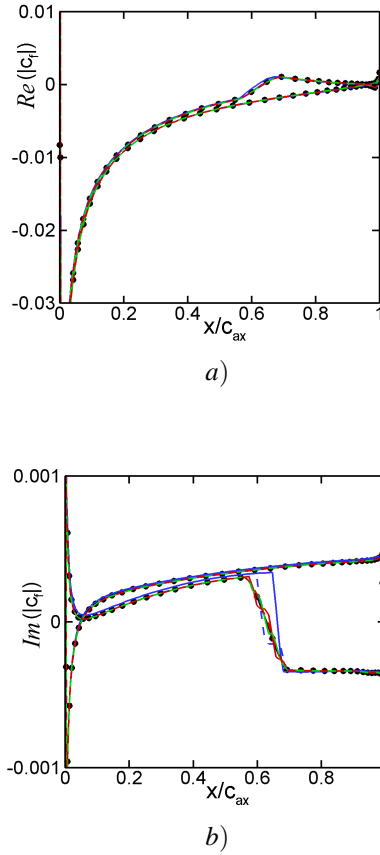
Figure 8. SKIN FRICTION COEFFICIENT OF 90 % BLADE SECTION COMPUTED WITH TD AND FIVE HB ANALYSES (LINE LEGEND AS IN FIG. 7-a): a) REAL PART, b) IMAGINARY PART.

approximation proportional to $2N_H + 1$. The HB *speed up* parameter, defined as the ratio of the wallclock time required to calculate three periods with the TD solver and a single period with the HB solver for each of the adopted five values of N_H is reported in Table 2. The first row of speed up parameters refers to results computed using the aforementioned residual tolerance l_r of $1.d - 12$, and it shows that the accurate HB solution obtained with $N_H = 3$ can be obtained 17 times faster than with the TD analysis reported herein. The blade forces, however, may achieve an acceptable level of convergence with less stringent residual tolerances. Indeed, comparing the results of the TD simulation with $l_r = 1.d - 12$ and that with $l_r = 1.d - 09$ reveals that the maximum difference of the lift and drag coefficients with respect to their averages over the third period computed with $l_r = 1.d - 12$ is smaller than $1.d - 01\%$. Similarly, comparing the results of the HB simulations with $l_r = 1.d - 12$ and that with $l_r = 1.d - 09$ reveals that the maximum difference of the lift and drag coefficients with respect to their averages over the third period computed with $l_r = 1.d - 12$ is of order $1.d - 04\%$. The second row of speed up parameters of table 2 refers to results computed using residual tolerance l_r of $1.d - 09$, and it shows that the HB solution obtained with $N_H = 3$ can be obtained 8 times faster than with the TD analysis.
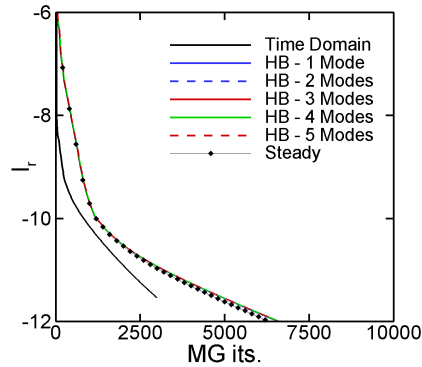
Figure 9. CONVERGENCE HISTORIES OF TD, HB AND STEADY ANALYSES FOR 90 % BLADE SECTION.

Table 2. ACCELERATION FACTORS OF HB ANALYSES WITH RESPECT TO TIME-DOMAIN ANALYSIS FOR THE 90 % BLADE SECTION.

l_r	N_H	1	2	3	4	5
1.d-12	speed up	40.8	24.3	17.4	13.5	11.0
1.d-09	speed up	19.3	11.4	8.2	6.3	5.2

Section at 30 % blade height

The flow regime associated with this section is more complex than that of the 90 % section, because the reduced frequency of the former is nearly 10 times that of the latter. The lift coefficient c_l over one rotor revolution computed by the TD analysis and five HB analysis with $N_H = 1, \ldots 5$ is depicted in Fig. 10. These curves show that an accurate prediction of c_l by means of the HB analysis is achieved with $N_H \geq 3$. More precisely, the HB solution obtained with $N_H = 3$ still presents some discrepancies with respect to the TD solution, whereas the HB solutions for $N_H = 4$ and $N_H = 5$ are practically superimposed on the TD solution. The plot also highlights that, unlike in the case of the 90 % section, c_l increases as ϕ_{fs} increases and viceversa. This happens because the flow does not separate, possibly due to the high value of λ, and therefore the airfoil response is closer to the steady ascending branch of a standard lift/AoA curve. The hysteresis cycles of c_l, c_d and c_m are depicted in the three plots of Fig. 11, the inspection of which confirms that the HB analyses with $N_H \geq 3$ lead to an excellent agreement with the TD result.

The real and imaginary part of c_p computed by the TD analysis and the five HB analyses are plotted in Figures 12-a and 12-b respectively. These figures may lead one to believe that 2 harmonics are sufficient to resolve the flow unsteadiness with the HB analysis, particularly if one considers the real part of c_p. These plots, however, show only the first harmonic of the unsteady flow. The fact that the hysteresis force loops highlight that 2 harmonics are not sufficient to fully resolve the periodic unsteady flow highlights that a non-negligible contribution of the second harmonic is present. Since one of the main output functionals of the yawed wind analysis is the time-dependent force at the attachment of the blade root to the rotor hub, the contribution of the higher order harmonics cannot be
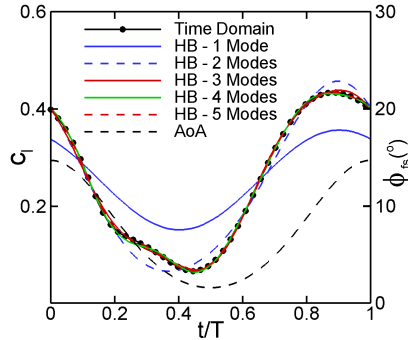
Figure 10. LIFT COEFFICIENT OF 30 % BLADE SECTION OVER ONE REVOLUTION COMPUTED WITH TD AND FIVE HB ANALYSES.

neglected in practical applications, as doing so may result in the inaccurate estimate of the time-dependent structural stress at the blade attachment. The real and imaginary part of the absolute value of c_f computed by the TD analysis and the 5 HB analyses are provided in Figures 13-a and 13-b respectively. The plot of the imaginary part shows more clearly that at least 3 harmonics are required in order to fully capture the viscous unsteady characteristics of this problem.

The convergence histories of the five HB analyses and that of the TD solver for a particular physical time are reported in Fig. 14. As for the section at 90 % blade height, the HB analyses have been run until $l_r \leq 1.d - 12$; the iterative solution process of each physical time-step of the TD analysis has been stopped either when $l_r \leq 1.d - 12$ or after 3000 MG iterations if at this stage this convergence tolerance had not been achieved. For most physical time-steps, the prescribed residual tolerance of $1.d - 12$ has been achieved using all 3000 MG iterations. Unlike the case of the 90 % blade section, one now sees that the convergence histories of the 5 HB analyses are not superimposed, and the convergence rate of the HB analyses appears to decrease as N_H increases. Figure 14 also reports the convergence history for the steady problem, which shows that the steady solver converges to the required level of convergence using fewer iterations than all HB analyses. A closer inspection of this figure reveals that the asymptotic convergence rate (*i.e.* the constant slope of the residual curves after the initial numerical transient) of the steady and the HB solver is about the smae. As discussed in the section on the integration of the HB equations, these patterns may be due to a significant nonlinearity of the unsteady flow, which results in a large contribution of the HB source terms to the overall HB Jacobian. Such contribution may increase the non-normality of the HB Jacobian with respect to that of the steady equations, resulting in an initially slower decay of the HB residuals. The analysis of the sectional forces has highlighted that not only the first but also the higher order harmonics contribute to this unsteady flow. Therefore, the non-normality of the HB Jacobian is likely to increase with N_H, which may explain the increasing reduction of the initial convergence rate as N_H is increased. The higher nonlinearity of the flow field of the 30 percent section with respect to that of the 90 percent section is caused primarily by the higher reduced frequency of the motion of the former section. It is the authors' experience that the abovesaid dependence of the HB convergence rate on N_H always increases with the flow nonlinearities. As with the 90 percent blade section, these HB analyses could be performed without the RK stabilization previously discussed, namely using algorithm (28) for the solution update. It has also been verified that the use of the stabilized integration (29) results in negligible changes of the convergence history of the 5 HB
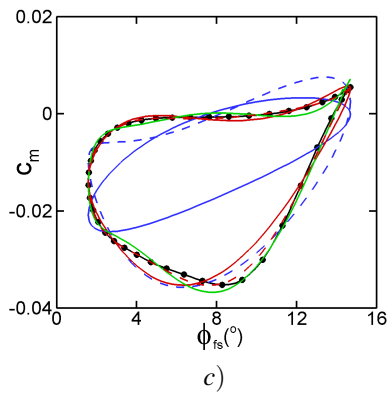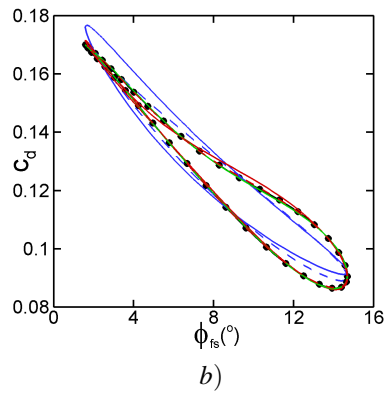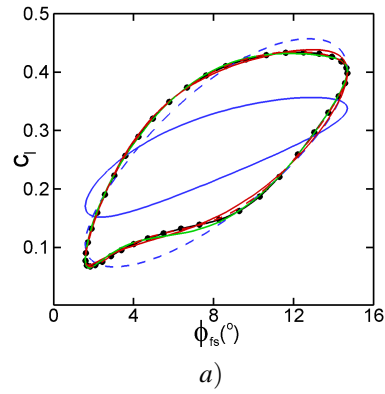
a)

b)

c)

Figure 11.   HYSTERESIS FORCE LOOPS OF 30 % BLADE SECTION COMPUTED WITH TD AND FIVE HB ANALYSES (LINE LEGEND AS IN FIG. 10): a) LIFT COEFFICIENT, b) DRAG COEFFICIENT, c) PITCHING MOMENT COEFFICIENT.

analyses with respect to the curves of Fig. 14. The HB speed up parameter is reported in Table 3. One sees that the accurate HB solution obtained with $N_H = 4$ can be obtained more than 10 times faster than with the TD analysis reported herein. Similarly to what done in
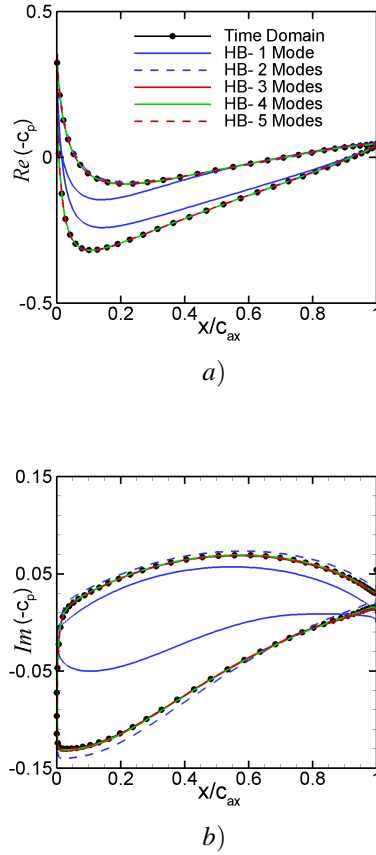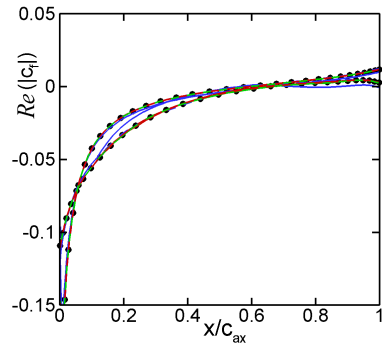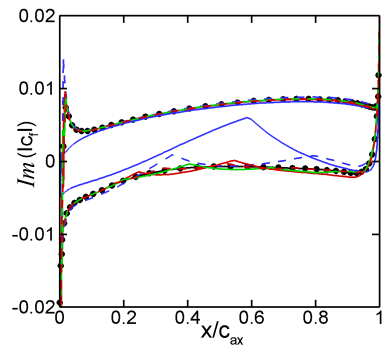
Figure 12. PRESSURE COEFFICIENT OF 30 % BLADE SECTION COMPUTED WITH TD AND FIVE HB ANALYSES: a) REAL PART, b) IMAGINARY PART.

the case of the 90 percent blade section, the speed up parameters corresponding to the analyses performed with $l_r = 1.d - 09$ have also been considered. Comparing the results of the TD simulation with $l_r = 1.d - 12$ and that with $l_r = 1.d - 09$ reveals that the maximum difference of the lift and drag coefficients with respect to their averages over the third period computed with $l_r = 1.d - 12$ is smaller than $1.d - 01\%$. Similarly, comparing the results of the HB simulations with $l_r = 1.d - 12$ and that with $l_r = 1.d - 09$ reveals that the maximum difference of the lift and drag coefficients with respect to their averages over the third period computed with $l_r = 1.d - 12$ is of order $1.d - 01\%$. The second row of speed up parameters of table 3 refers to results computed using residual tolerance l_r of $1.d - 09$, and it shows that the HB solution obtained with $N_H = 4$ can be obtained 8 times faster than with the TD analysis.

The quantitative effects of LSP on the estimate of the sectional lift force are assessed in the plot of Fig. 15, the abscissas of which report time as a fraction of a period. The left ordinates report the lift coefficient computed using LSP, and the right ordinates report the absolute value of the percentage error between the lift coefficient computed with LSP and that computed without. One sees that the maximum error is above 4 %. The inaccuracy of the prediction without LSP grows as the Mach number decreases. In the case

TURBO-10-1073, M.S. Campobasso

a)

b)

Figure 13. SKIN FRICTION COEFFICIENT OF 30 % BLADE SECTION COMPUTED WITH TD AND FIVE HB ANALYSES (LINE LEGEND AS IN FIG. 12-a): a) REAL PART, b) IMAGINARY PART.
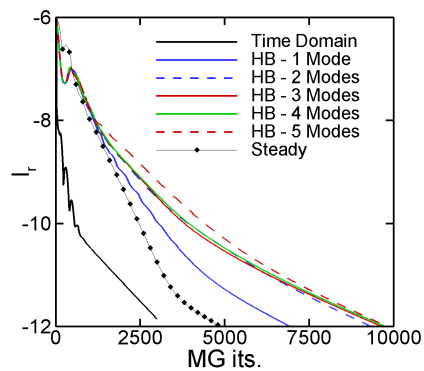

Figure 14. CONVERGENCE HISTORIES OF TD, HB AND STEADY ANALYSES FOR 30 % BLADE SECTION.

Table 3. ACCELERATION FACTORS OF HB ANALYSES WITH RESPECT TO TIME-DOMAIN ANALYSIS FOR THE 30 % BLADE SECTION.

l_r	N_H	1	2	3	4	5
1.d-12	speed up	48.1	22.4	16.0	12.4	10.2
1.d-09	speed up	30.7	15.3	10.6	8.1	6.2

of turbulent conditions the inaccuracies due to the lack of LSP become even larger, and they may lead to significantly different stall characteristics of the section [34].
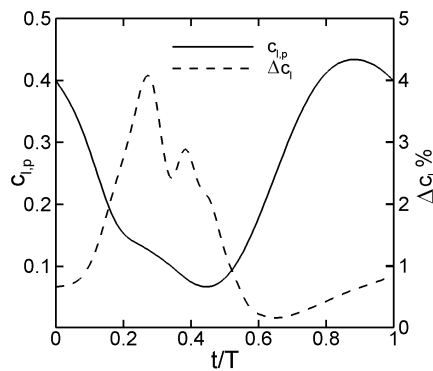

Figure 15. LIFT COEFFICIENT OF 30 % BLADE SECTION COMPUTED BY TD ANALYSIS WITH AND WITHOUT LOW-SPEED PRECONDITIONING.

CONCLUSIONS

The numerical models underlying the implementation of a novel harmonic balance compressible Navier-Stokes solver with low-speed preconditioning for wind turbine unsteady aerodynamics have been presented. The integration of both the harmonic balance and the time-domain equations is based on a multigrid iteration using a multi-stage Runge-Kutta smoother, and including local time-stepping and implicit residual smoothing for further convergence acceleration. In the framework of the dual-time stepping method used for solving the time-domain problem, the explicit multigrid integration can present a numerical instability when the local pseudo-time-step is much larger than the physical time-step. Previous experience of the authors with the harmonic balance solver described in this paper lead one to believe that a numerical instability of similar origin can also arise when using the same multigrid approach for the solution of the harmonic balance equations. Therefore, a novel stabilization procedure for the multigrid integration of the HB NS equations has been designed and presented herein. The harmonic balance solver with low-speed preconditioning is well suited for the analyses of periodic wind turbine flows. The computational performance and the accuracy of the technology being developed have been assessed by computing the flow field past two sections of a horizontal axis wind turbine blade in yawed wind with both the

time- and frequency-domain solvers. Results highlight that the harmonic balance solver features accuracies comparable to those of its time-domain counterpart, and yields a reduction of computational costs of about one order of magnitude with respect to the time-domain solver. The aerodynamic analyses presented herein are laminar and two-dimensional. A substantially larger reduction of computational times is expected for the case of periodic turbulent three-dimensional flows. The time-domain analysis of these problems, in fact, is likely to require a higher time-resolution per period and possibly a larger number of cycles before a periodic state is achieved. In these circumstances the benefits of using the harmonic balance technology will be even higher than those reported in this paper.

ACKNOWLEDGMENT

REFERENCES

[1] Hansen, M., Sorensen, J., Voutsinas, S., Sorensen, N., and Madsen, H., 2006. "State of the art in wind turbine aerodynamics and aeroelasticity". *Progress in Aerospace Sciences, 42*, pp. 285–330.

[2] Gomez-Iradi, S., Steijl, R., and Barakos, G., 2009. "Development and Validation of a CFD Technique for the Aerodynamic Analysis of HAWT". *Journal of Solar Energy Engineering, 31*(8), August.

[3] Le Pape, A., and Gleize, V., 2006. Improved Navier-Stokes Computations of a Stall-regulated Wind Turbine Using Low Mach Number Preconditioning. AIAA paper 2006-1502, January. 44th AIAA Aerospace Sciences Meeting and Exhibit, Reno, Nevada.

[4] Sorensen, N., Michelsen, J., and Schreck, S., 2002. "Navier-Stokes Predictions of the NREL Phase VI Rotor in the NASA Aimes 80 ft × 120 ft Wind Tunnel". *Wind Energy, 5*, pp. 151–169.

[5] Madsen, H., Sorensen, N., and Schreck, S., 2003. Yaw Aerodynamics Analyzed with Three Codes in Comparison with Experiments. AIAA paper 2003-0519.

[6] Hall, K., Thomas, J., and Clark, W., 2002. "Computations of unsteady nonlinear flows in cascades using a harmonic balance technique". *AIAA Journal, 40*(5), May, pp. 879–886.

[7] Su, X., and Yuan, X., 2010. "Implicit Solution of Time-Spectral Method for Periodic Unsteady Flows". *International Journal for Numerical Methods in Fluids, 63*(7), pp. 860–876.

[8] van der Weide, E., Gopinath, A., and Jameson, A., 2005. Turbomachinery Applications with the Time Spectral Method. AIAA paper 2005-4905, June. 17th AIAA Computational Fluid Dynamics Conference, Torontp, Ontario, Canada.

[9] Da Ronch, A., Choreyshi, M., Badcock, K., Goertz, S., Widhalm, M., Dwight, R., and Campobasso, M., 2010. Linear Fre-

quency Domain and Harmonic Balance Predictions of Dynamic Derivatives. AIAA paper 2010-4699, July. 28th AIAA Applied Aerodynamics Conference, Chicago, Illinois.

[10] Sicot, F., Puigt, G., and Montagnac, M., 2008. "Block-Jacobi Implicit Algorithms for the Time Spectral Method". *AIAA Journal, 46*(12), December, pp. 3080–3089.

[11] Woodgate, M. A., and Badcock, K. J., 2009. "Implicit Harmonic Balance Solver for Transonic Flows with Forced Motions". *AIAA Journal, 47*(4), April, pp. 893–901.

[12] McMullen, M., and Jameson, A., 2006. "The computational efficiency of non-linear frequency domain methods". *Journal of Computational Physics, 212*(2), pp. 637–661.

[13] McMullen, M., Jameson, A., and Alonso, J., 2002. Application of a Non-linear Frequency-domain Solver to the Euler and Navier-Stokes Equations. AIAA paper 2002-0120, January. 40th AIAA Aerospace Sciences Meeting and Exhibit, Reno, Nevada.

[14] McMullen, M., Jameson, A., and Alonso, J., 2001. Acceleration of convergence to a periodic steady state in turbomachinery flows. AIAA paper 2001-0152, January. 39th AIAA Aerospace Sciences Meeting and Exhibit, Reno, Nevada.

[15] Kumar, M., and Murthy, V., 2006. Rotor Blade Response Based on CFD in the Frequency Domain. AIAA paper 2006-438, January. 44th AIAA Aerospace Sciences Meeting and Exhibit, Reno, Nevada.

[16] He, L., 2008. "Harmonic Solution of Unsteady Flow Around Blades with Separation". *AIAA Journal, 46*(6), June, pp. 1299–1307.

[17] Venkateswaran, S., and Merkle, C., 1999. "Analysis of preconditioning methods for the Euler and Navier-Stokes equations". *30th VKI Lecture Series on Computational Fluid Dynamics*.

[18] Campobasso, M., Bonfiglioli, A., and Baba-Ahmadi, M., 2009. "Development of Efficient and Accurate CFD Technologies for Wind Turbine Unsteady Aerodynamics". In Proceedings of the Conference on Modeling Fluid Flow, J. Vad, ed., Vol. **2** of *14th Event of International Conference Series on Fluid Flow Technologies held in Budapest*, Department of Fluid Mechanics, Budapest University of Technology and Economics, pp. 879–886.

[19] Liu, L., Thomas, J., Dowell, E., Attar, P., and Hall, K., 2006. "A comparison of classical and high dimensional harmonic balance approaches for a Duffing oscillator". *Journal of Computational Physics, 215*(1), pp. 298–320.

[20] Campobasso, M., and Baba-Ahmadi, M., 2011. "Ad-hoc Boundary Conditions for CFD Analyses of Turbomachinery Problems with Strong Flow Gradients at Farfield Boundaries". *Journal of Turbomachinery, 133*(4).

[21] Jackson, A., Campobasso, M., and Baba-Ahmadi, M., 2011. On the Parallelization of a Harmonic Balance Compressible Navier-Stokes Solver for Wind Turbine Aerodynamics. ASME paper GT2011-45306.

[22] Jameson, A., 1991. Time Dependent Calculations Using Multigrid, with Applications to Unsteady Flows Past Airfoils and Wings. AIAA paper 91-1596.

[23] Arnone, A., Liou, M.-S., and Povinelli, L., 1993. Multigrid Time-Accurate Integration of Navier-Stokes Equations. Technical Memorandum NASA TM 106373, ICOMP-93-37, Lewis Research Center, Cleveland, OH, USA, November.

[24] Melson, N., Sanetrik, D., and Atkins, H., 1993. "Time-accurate Navier-Stokes calculations with multigrid acceleration". *Proc. 6th*

Copper mountain Conference on Multigrid Methods, pp. II423–II437.

[25] Briggs, W., Henson, V., and McCormick, S., 2000. *A Multigrid Tutorial, Second edition*. SIAM, Philadelphia, USA.

[26] Threfethen, L., and Embree, M., 2005. *Spectra and Pseudospactra*. Princeton University Press, Princeton, New Jersey.

[27] Thomas, J., Duster, C., Dowell, E., and Hall, K., 2009. Unsteady Flow Computation Using a Harmonic Balance Approach Implemented About the OVERFLOW 2 Flow Solver. AIAA paper 2009-4270, June. 19th AIAA Computational Fluid Dynamics Conference, San Antonio, Texas.

[28] Weiss, J., Maruszewski, J., and Smith, W., 1999. "Implicit Solution of Preconditioned Navier-Stokes Equations Using Algebraic Multigrid". *AIAA Journal, 37*(1).

[29] Darmofal, D., and Siu, K., 1999. "A robust multigrid algorithm for the Euler equations with local preconditioning and semi-coarsening". *Journal of Computational Physics, 151*, pp. 728–756.

[30] Buelow, P., 1995. "Convergence Enhancement of Euler and Navier-Stokes Algorithms". PhD thesis, Pennsylvania State University, Pennsylvania, USA, December.

[31] Pandya, S., Venkateswaran, S., and Pulliam, T., 2003. "Implementation of dual-time procedures in overflow". *Technical Report AIAA-2003-0072*.

[32] Bonfiglioli, A., Campobasso, M., and Carpentieri, B., 2009. Parallel Unstructured Three-dimensional Turbulent Flow Analyses Using Efficiently Preconditioned Newton-Krylov Solver. AIAA paper 2009-4137, June. 19th AIAA Computational Fluid Dynamics Conference, San Antonio, Texas.

[33] Theodorsen, T., 1935. General Theory of Aerodynamic Instability and the Mechanism of Flutter. Tech. Rep. NACA Report 496.

[34] Le Pape, A., and J.Lecanu, 2004. "3D Navier-Stokes computations of a stall-regulated wind turbine". *Wind Energy, 7*, pp. 309–324.

LIST OF TABLE CAPTIONS

TABLE 1: INPUT PARAMETERS FOR THE 2D UNSTEADY MOVING-GRID CFD ANALYSES OF TWO SECTIONS OF HAWT BLADE.

TABLE 2: ACCELERATION FACTORS OF HB ANALYSES WITH RESPECT TO TIME-DOMAIN ANALYSIS FOR THE 90 % BLADE SECTION.

TABLE 3: ACCELERATION FACTORS OF HB ANALYSES WITH RESPECT TO TIME-DOMAIN ANALYSIS FOR THE 30 % BLADE SECTION.

LIST OF FIGURE CAPTIONS

FIGURE 1: SCHEMATIC VIEWS OF HAWT IN YAWED WIND. LEFT PLOT: TOP VIEW; RIGHT PLOT: FRONT VIEW.

FIGURE 2: VELOCITY TRIANGLES OF HAWT BLADE SECTION FOR POSITIONS LABELED *A* TO *D* IN FIG. 1.

FIGURE 3: HARMONIC MOTION OF HAWT BLADE SECTION CORRESPONDING TO YAWED INFLOW.

FIGURE 4: AMPLITUDE OF THE FIRST HARMONIC OF THE DIFFERENTIAL STATIC PRESSURE COEFFICIENT ACROSS A PITCHING FLAT PLATE: COMPARISON OF THEORETICAL RESULT AND NUMERICAL PREDICTIONS OBTAINED WITH AND WITHOUT LSP.

FIGURE 5: LIFT COEFFICIENT OF 90 % BLADE SECTION OVER ONE REVOLUTION COMPUTED WITH TD AND FIVE HB ANALYSES.

FIGURE 6: HYSTERESIS FORCE LOOPS OF 90 % BLADE SECTION COMPUTED WITH TD AND FIVE HB ANALYSES (LINE LEGEND AS IN FIG. 5): a) LIFT COEFFICIENT, b) DRAG COEFFICIENT, c) PITCHING MOMENT COEFFICIENT.

FIGURE 7: PRESSURE COEFFICIENT OF 90 % BLADE SECTION COMPUTED WITH TD AND FIVE HB ANALYSES: a) REAL PART, b) IMAGINARY PART.

FIGURE 8: SKIN FRICTION COEFFICIENT OF 90 % BLADE SECTION COMPUTED WITH TD AND FIVE HB ANALYSES (LINE LEGEND AS IN FIG. 7-a): a) REAL PART, b) IMAGINARY PART.

FIGURE 9: CONVERGENCE HISTORIES OF TD, HB AND STEADY ANALYSES FOR 90 % BLADE SECTION.

FIGURE 10: LIFT COEFFICIENT OF 30 % BLADE SECTION OVER ONE REVOLUTION COMPUTED WITH TD AND FIVE HB ANALYSES.

FIGURE 11: HYSTERESIS FORCE LOOPS OF 30 % BLADE SECTION COMPUTED WITH TD AND FIVE HB ANALYSES (LINE LEGEND AS IN FIG.10): a) LIFT COEFFICIENT, b) DRAG COEFFICIENT, c) PITCHING MOMENT COEFFICIENT.

FIGURE 12: PRESSURE COEFFICIENT OF 30 % BLADE SECTION COMPUTED WITH TD AND FIVE HB ANALYSES: a) REAL PART, b) IMAGINARY PART.

FIGURE 13: SKIN FRICTION COEFFICIENT OF 30 % BLADE SECTION COMPUTED WITH TD AND FIVE HB ANALYSES (LINE LEGEND AS IN FIG. 12-a): a) REAL PART, b) IMAGINARY PART.

FIGURE 14: CONVERGENCE HISTORIES OF TD, HB AND STEADY ANALYSES FOR 30 % BLADE SECTION.

FIGURE 15: LIFT COEFFICIENT OF 30 % BLADE SECTION COMPUTED BY TD ANALYSIS WITH AND WITHOUT LOW-SPEED PRECONDITIONING.